Japanese guideline for the oncology FDG-PET/CT data acquisition protocol: synopsis of Version 1.0 (the Guideline) based on the results of the phantom experiments performed by the Core Laboratory.

Results A total of 18 centers (19 scanners) participated in this trial. The center's default protocol was unchanged for 9 scanners (47.4 %) and changed for 10 scanners (52.6 %). Both acquisition duration and reconstruction parameters were changed in 3 (15.8 %) of 10 scanners and the acquisition duration alone was changed in 7 (36.8 %) scanners. Also, the accuracy of the standardized uptake value (SUV) was evaluated with the acceptable level 1.0 ± 0.1, resulting in readjustment and recalibration in 2 scanners (10.5 %), which were confirmed to attain the acceptable accuracy after the required readjustment. As of August 2012, 21 patients have undergone an FDG-PET/CT examination under the acquisition protocols determined by the Core Laboratory. Evaluation of the image quality using several physical parameters confirmed that the accumulated data were of sufficient quality.

Conclusions Optimization of the acquisition protocol, in compliance with the guideline, was successfully achieved by the Core Laboratory in the framework of JSCT NHL10 to accumulate equivalent quality data across multiple centers. The progress of the trial was greatly facilitated by support from the Japan Society of Nuclear Medicine Working Group for Investigation of Response Evaluation Criteria in Malignant Tumors Using Standardized PET/CT (Principal Investigator: Ukihide Tateishi, MD., PhD).

Keywords FDG · PET/CT · Diffuse large B cell lymphoma · Standardization · Multicenter study

Introduction

Positron emission tomography (PET) using 2-fluorine-18-fluoro-2-deoxy-D glucose (FDG) is an indispensable imaging modality for diagnosing malignant lymphoma. FDG-PET imaging has been reported to be effective in staging and evaluating the response to treatment. Its effectiveness in monitoring post-treatment recurrence/exacerbation and evaluating the prognosis at mid-therapy was recently investigated in a clinical trial [1].

FDG-PET is performed during treatment of diffuse large B cell lymphoma (DLBCL) because the response to treatment revealed by FDG-PET images can reflect prognosis. If FDG-PET images show a poor response after treatment, the planned treatment can potentially be altered to improve the outcome [2–4]. On the basis of this hypothesis, several stratified clinical trials were performed on patients with

aggressive lymphoma with a poor prognosis. Aggressive chemotherapy or high-dose chemotherapy in combination with autotransplantation was employed when FDG-PET revealed a poor response to treatment [5, 6].

However, the data from several reports do not support the correlation between mid-therapy FDG-PET observations and prognosis [7]. One of the possible reasons for the negative results may be related to the details of FDG-PET data acquisition and assessment [8].

In Japan, a multicenter trial, "Japan Study Group for Cell Therapy and Transplantation (JSCT) NHL 10", is underway to investigate the effectiveness and safety of a stratified treatment protocol, in which high-risk CD20 positive DLBCL patients undergo two courses of R-CHOP chemotherapy before evaluation by FDG-PET. Patients with poor response to treatment (positive cases) receive high-dose chemotherapy followed by autologous stem cell transplantation (PET positive treatment) while patients with sufficient response to treatment (negative patients) receive eight courses of R-CHOP chemotherapy (PET negative treatment).

FDG-PET image quality depends on many factors including scanner type, administered dose, acquisition protocol, and image reconstruction parameters. Therefore, the quality of the PET images between multiple centers can only be guaranteed through standardization of the imaging parameters and appropriate quality control (QC) of the scanners. In the US, the Clinical Trial Network (CTN) organized by the Society of Nuclear Medicine (SNM) is attempting to standardize the synthesis of PET radiopharmaceuticals and the scanning protocol [9]. In addition to the CTN, the American College of Radiology Imaging Network (ACRIN) [10] is active in the field and the European Association of Nuclear Medicine (EANM) operates a similar network [8]. However, a network that focuses on standardizing image quality through scanning protocols or QC of the acquired data is still under development in Japan [11].

Japanese guideline for the oncology FDG-PET/CT data acquisition protocol: synopsis of Version 1.0 (the Guideline) was established [12], though there is no Core Laboratory to promote standardization that is comparable to those in the US and Europe. As a result, we established a trial-specific Core Laboratory for JSCT NHL10 comprising two board certified PET nuclear medicine physicians and three board certified nuclear medicine technologists. The purpose of the laboratory was to standardize FDG-PET image quality and quantification on the basis of the guideline, as well as to evaluate the validity of the standardization. This report describes the procedure and result of this attempt. The Japan Society of Nuclear Medicine Working Group for Investigation of Response Evaluation Criteria in Malignant Tumors Using Standardized PET/CT

(Principal Investigator: Ukihide Tateishi, MD., PhD) jointly conducted this study.

Materials and methods

Accreditation of the PET/CT scanners and determination of data acquisition protocol

The Core Laboratory was utilized to determine if FDG-PET data were acquired under appropriate conditions and if appropriate QC was implemented for the scanner. To ascertain the validity of the acquisition protocol and image reconstruction parameters, phantom experiments were conducted in compliance with the guideline. The investigated items were: (1) scanner manufacturer and model type; (2) frequency and content of QC; (3) availability of FDG; (4) injection method; (5) injected dose; (6) uptake duration; (7) data acquisition mode; (8) scan duration; (9) availability of list mode; (10) image reconstruction method; (11) image reconstruction parameters; (12) history of phantom experiments; and (13) evaluation of phantom experiment results. If possible, centers provided existing phantom experimental data to the Core Laboratory. In centers with no existing phantom experimental data, center's staff carried out the experiment and/or Core Laboratory members visited the centers to provide technical support during acquisition of phantom experiment data.

The National Electrical Manufacturers Association (NEMA) standards body phantom [13] and ^{18}F-solution were used as part of experiments in which PET data on a simulated torso of the human body were acquired with varied scan duration. The obtained images were both physically and visually evaluated. Phantom background activity concentration was controlled at 2.65 kBq/ml and the hot sphere activity was controlled at four times the background activity. Emission scan duration was 12 min with three-dimensional (3D) list-mode acquisition. When the list mode was not available, the default acquisition duration used in the clinical PET/CT examinations was used to acquire the data. Computed tomography (CT) for attenuation correction was performed with default acquisition parameters of each center. List-mode data were histogramed into a sinogram of 1–10 min/bed position and the image was reconstructed by the center's default method and parameters.

Phantom data were stored in the DICOM format and submitted to the Core Laboratory. PET images submitted to the Core Laboratory were viewed with the viewer OsiriX MD for physical analysis. Then, the phantom noise equivalent count ($NEC_{phantom}$), visualization of the 10-mm sphere (visual score), image noise (N_{10mm}), % contrast ($Q_{H,10mm}/N_{10mm}$), and relative recovery coefficient (RC) were evaluated and compared with the reference values recommended in the Guideline [12]. Visualization of the 10-mm sphere was evaluated in the Core Laboratory. On the basis of these analyses of phantom data, the imaging conditions recommended for the clinical trial were determined for each scanner.

Although the guideline does not provide any recommendations regarding the accuracy of the SUV, the values were obtained for 12 regions of interest (ROIs) defined in the background area of a phantom image with a 30-min scan duration to evaluate accuracy with an acceptable level of 1.0 ± 0.1 [10].

### Quality assurance of the patient data

As of August 2012, 21 patients have undergone FDG-PET examination with the acquisition conditions determined on the basis of phantom experiments (Table 1). The institutional review board approved the investigations in each center. All patients gave informed consents. The patient group comprised 11 males and 10 females with a mean height of 160.7 ± 9.6 cm (range 146.4–185.0 cm), a mean weight of 50.5 ± 11.2 kg (range 31.6–73.0 kg), and a body mass index (BMI) of 19.4 ± 3.0 kg/m^2 (range 13.2–25.0 kg/m^2). The mean administered dose was 270.5 ± 38.4 MBq (range 211.0–324.8 MBq), while uptake duration was 60.3 ± 2.6 min (54.0–64.0 min), and blood glucose level was 103.0 ± 10.6 mg/dl (89.0–117.0 mg/dl). Patient image data were submitted to the Core Laboratory immediately after examination to check for the presence of artifacts attributable to the scanner, body movement during examination, or poor registration of the PET and CT images. The patient noise equivalent count ($NEC_{patient}$), patient noise equivalent count density ($NEC_{density}$), and mean signal-to-noise ratio (SNR) within the liver ROI (liver SNR) were determined to establish if the patient data were in compliance with the Guideline.

Results

A total of 18 centers (19 scanners) were enrolled in this trial (Table 1). Only one center had conducted phantom experiments to determine the scan and image reconstruction conditions before participation in this trial. The other 17 centers carried out the phantom experiments especially for this trial. One of the centers performed the phantom experiment independently while the others had support from the Core Laboratory members who performed the phantom experiments and obtained the data. The following PET/CT models were used: General Electric—3 Discovery STs, 3 Discovery STEPs, 4 Discovery STEs, and 1 Discovery 690; Siemens—4 Biographs, 1 Biograph True

Table 1 List of center, prefecture, scanner and number of patients

No.	Center	Prefecture	Scanner	Number of patients
1	Anjo Kosei Hp.	Aichi	Biograph 16 (Siemens)	
2	Central CI clinic Hp.	Hokkaido	Discovery STEP (GE)	
3	Gifu Univ. Hp.	Gifu	Biograph 16 (Siemens)	2
4	Ehime Pref. Central Hp.	Ehime	Discovery STE (GE)	
5	Kusunoki Hp.	Gunma	Discovery ST (GE)	3
6	National Tokyo Medical Center	Tokyo	Biograph 40 (Siemens)	
7	Sapporo Goryokaku Hp.	Hokkaido	Discovery STEP (GE)	
8	Sapporo Medical Univ. Hp.	Hokkaido	Discovery STEP (GE)	1
9	Kameda Clinic Hp.	Kanagawa	Discovery STE (GE)	
10	Toranomon Hp.	Tokyo	Aquiduo (Toshiba)	
11	Kawasaki Medical Univ. Hp.	Okayama	Discovery STE (GE)	5
12	Kyushu Univ. Hp.	Fukuoka	Discovery STE (GE)	6
13	Kyushu Univ. Hp.	Fukuoka	Biograph mCT (Siemens)	
14	Oike Clinic	Kyoto	Biograph 64 (Siemens)	
15	Izumo City Hp.	Shimane	True Point Biograph 64 (Siemens)	
16	Kurume Univ. Hp.	Fukuoka	GEMINI GX-L (Philips)	4
17	Kanazawa Advanced Medical Center	Kanazawa	Discovery 690 (GE)	
18	Takinomiya General Hp.	Kagawa	Discovery ST (GE)	
19	Kusatsu General Hp.	Shiga	Discovery ST (GE)	
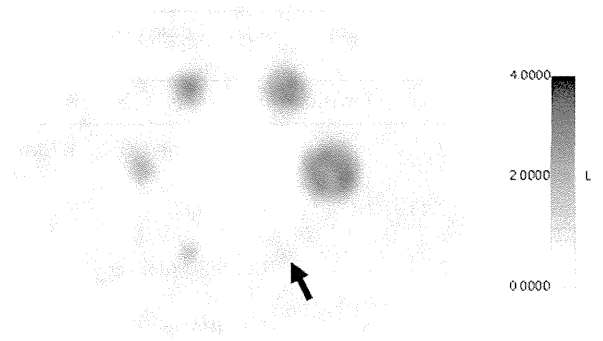
Fig. 1 Example of a phantom image that could not visualize a 10-mm hot sphere with a SUV = 4
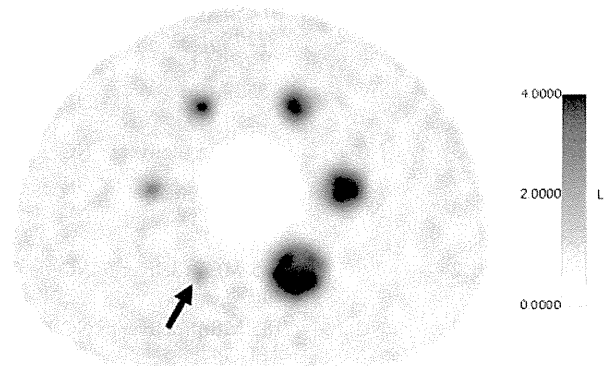
Fig. 2 Example of a phantom image that visualized a 10-mm hot sphere with a SUV = 4

Point, 1 Biograph mCT; Philips—1 GEMINI GX-L; and Toshiba Medical—1 Aquiduo.

Analysis by the Core Laboratory confirmed visualization of a 10-mm hot sphere in 9 scanners (47.4 %) with the respective centers' own clinical default settings without a need for modification. Examples of the phantom images that could and could not visualize the 10-mm hot sphere are shown in Figs. 1 and 2, respectively. Three scanners required modification of the scan duration and image reconstruction parameters (15.8 %), and 7 scanners

Fig. 3 Phantom images that **a** initially could not visualize a 10-mm hot sphere with a SUV = 4 and **b** visualized the hot sphere after the conditions were revised. The protocol revisions included changes in the scan duration from 2 min to 4 min/bed and image reconstruction parameters from 2 iterations to 3 iterations
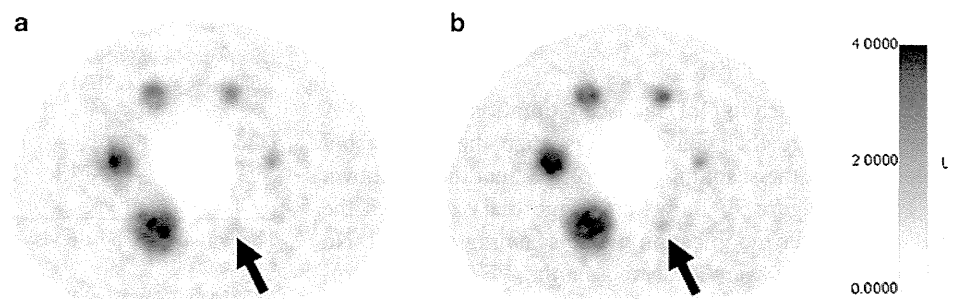
Table 2 List of scanners, scan durations and injected dose

Scanner	Scan duration (min)		Injected dose (MBq/kg or MBq)	
	Initial	Revision	Initial	Revision
Biograph Sensation16	2	3	3.0 MBq/kg	3.7 MBq/kg
Discovery STEP	2.43	NC	4.5 MBq/kg	NC
Biograph 16	2	4	185 MBq (deliver FDG)	NC
Discovery STE	3	NC	3.0 MBq/kg	3.7 MBq/kg
Discovery ST	2	4	185 MBq (deliver FDG)	NC
Biograph 40	3	4	185 MBq (deliver FDG)	NC
Discovery STEP	3	NC	185 MBq (<50 kg), 220 MBq (50–80 kg), 260 MBq (>80 kg)	3.7 MBq/kg
Discovery STEP	3	NC	185 MBq (deliver FDG)	NC
Discovery STE	3	NC	4.3 MBq/kg	NC
Aquiduo	2	4	185 MBq (deliver FDG)	NC
Discovery STE	2	NC	185 MBq (deliver FDG)	NC
Discovery STE	3	NC	185 MBq (deliver FDG)	NC
Biograph mCT	2	NC	185 MBq (deliver FDG)	NC
Biograph 64	2	3	4.5 MBq/kg	NC
True Point Biograph 64	2	3	185 MBq (deliver FDG)	NC
GEMINI GX-L	2	4	4.4 MBq/kg	NC
Discovery 690	2	NC	4.0 MBq/kg	NC
Discovery ST	2.5	4	185 MBq (deliver FDG)	NC
Discovery ST	2	3	3.0 MBq/kg	3.7 MBq/kg

The initial and post-revision scan durations and injected doses are shown

NC No revision parameters

required modification of the scan duration (36.8 %). A phantom image that could not visualize the 10-mm hot sphere before the scanning protocol was modified is shown in Fig. 3a. Figure 3b shows an image that visualized the hot sphere after modification of the scanning protocol. No serious artifacts were observed in the PET images produced by any of the scanners.

Table 3 List of scanners, image reconstruction methods and parameters

Scanner	Image reconstruction		
	Method	Initial parameter	Revision parameter
Biograph 16	FORE-OSEM	iter:3, sub:8, filter: 5 mm, matrix:128	NC
Discovery STEP	VUE-POINT+	iter:2, sub:21, filter: 5.14 mm, matrix:128	NC
Biograph 16	FORE-OSEM	iter:2, sub:8, filter: 5 mm, matrix:256	iter:3, sub:8, filter: 5 mm, matrix:256
Discovery STE	VUE-POINT+	iter:2, sub:20, filter: 4.29 mm, matrix:128	NC
Discovery ST	FORE-OSEM	iter:5, sub:16, filter: 5.14 mm, matrix:128	NC
Biograph 40	FORE-OSEM	iter:4, sub:8, filter: 5 mm, matrix:168	NC
Discovery STEP	VUE-POINT+	iter:2, sub:21, filter: 6 mm, matrix:128	NC
Discovery STEP	VUE-POINT+	iter:2, sub:21, filter: 5.14 mm, matrix:128	NC
Discovery STE	VUE-POINT+	iter:2, sub:21, filter: 6 mm, matrix:128	NC
Aquiduo	FORE-OSEM	iter:4, sub:14, filter: 8 mm, matrix:128	NC
Discovery STE	VUE-POINT+	iter:2, sub:20, filter: 5.14 mm, matrix:128	NC
Discovery STE	VUE-POINT+	iter:2, sub:28, filter: 6 mm, matrix:128	NC
Biograph mCT	TrueX with TF	iter:2, sub:21, filter: 6 mm, matrix:256	NC
Biograph 64	FORE-OSEM	iter:3, sub:8, filter: 6.5 mm, matrix:168	iter:4, sub:8, filter: 6.5 mm, matrix:256
True Point Biograph 64	TrueX	iter:3, sub:21, filter: 4 mm, matrix:168	NC
GEMINI GX-L	LOR-RAMLA	smooth	HQ mode, sharp
Discovery 690	VUE-POINT FX	iter:2, sub:18, filter: 5 mm, matrix:128	NC
Discovery ST	FORE-OSEM	iter:4, sub:16, filter: 5.14 mm, matrix:128	NC
Discovery ST	FORE-OSEM	iter:5, sub:16, filter: 5.14 mm, matrix:128	NC

The initial and post-revision image reconstruction parameters are shown

NC No revision parameters

Fig. 4 Liver SNR in 21 cases
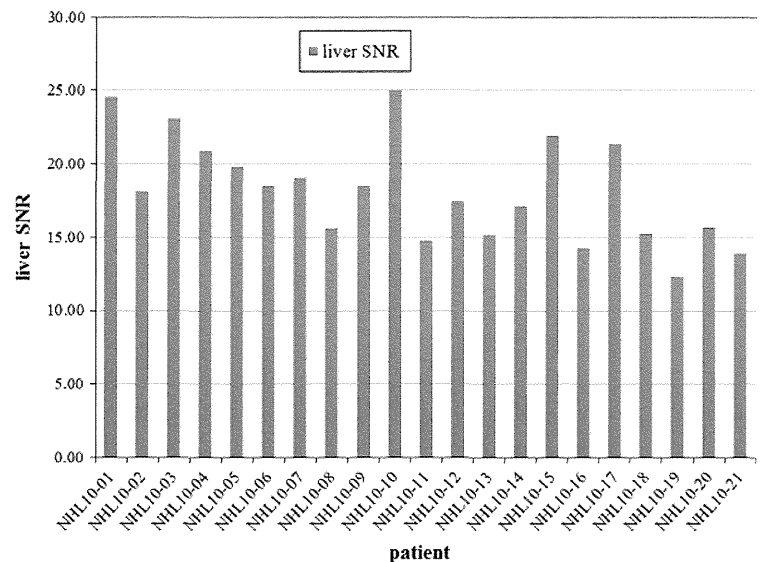
Fig. 5 NEC$_{density}$ in 21 cases
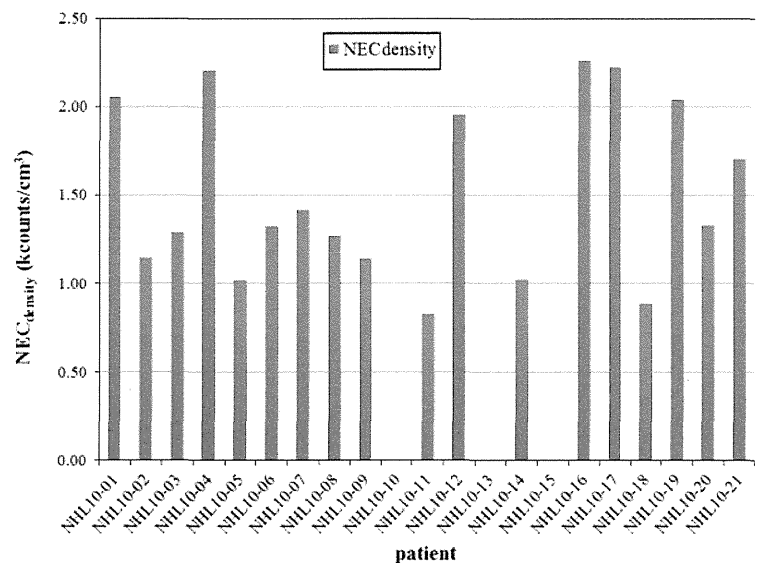
SUV was out of the acceptable range of 1.0 ± 0.1 in 2 scanners (10.5 %). Therefore, maintenance services including normalization, adjustment of gain value for the detector, QA of the dose calibrator, and recalibration were performed to ensure SUV accuracy. After this procedure, phantom data were acquired again and the SUV accuracy was confirmed to be within the acceptable range for this trial.

10-mm spheres were visualized in 3.1 ± 0.8 min on average (range 1–4 min). The mean physical indexes at that time were: $NEC_{phantom} = 7.7 \pm 2.4$ Mcounts (range 4.6–14.2 Mcounts), $N_{10mm} = 6.0 \pm 1.3$ % (range 4.3–9.3 %), $Q_{H,10mm} = 16.7 \pm 4.3$ % (range 10.4–24.2 %), $Q_{H,10mm}/N_{10mm} = 2.8 \pm 0.7$ (range 1.8–4.1). The mean relative RC for 10-mm sphere was 0.44 ± 0.05 (range 0.38–0.55). The mean background SUV was 0.97 ± 0.04

(range 0.92–1.05). The injected dose and scan duration of each scanner are shown in Table 2, and reconstruction methods with the parameters are shown in Table 3 with or without revision.

No significant artifact was observed within any of the acquired patient images and compliance with the protocol was confirmed with the header data in each PET image. With the mean $NEC_{patient} = 46.8 \pm 13.8$ Mcounts/m (range 31.4–75.5 Mcounts/m), mean $NEC_{density} = 1.21 \pm 0.45$ kcounts/cm^3 (range 0.69–2.21 kcounts/cm^3), and mean liver $SNR = 19.3 \pm 3.1$ (range 14.8–25.1), the physical indexes were in the reference ranges recommended in the Guideline (Figs. 4, 5, 6). Count data were not recorded in the DICOM header in three cases for which the liver SNR was used for confirmation. Typical clinical images with $NEC_{density} = 0.86$ (kcounts/cm^3),

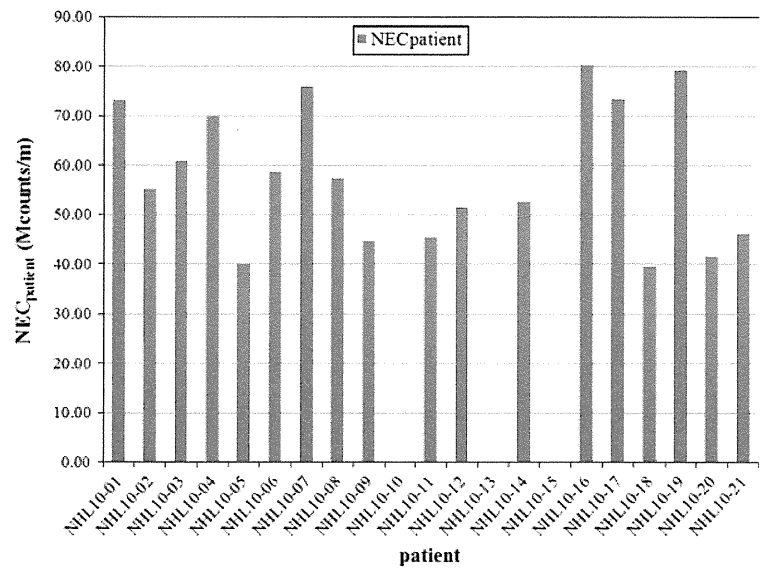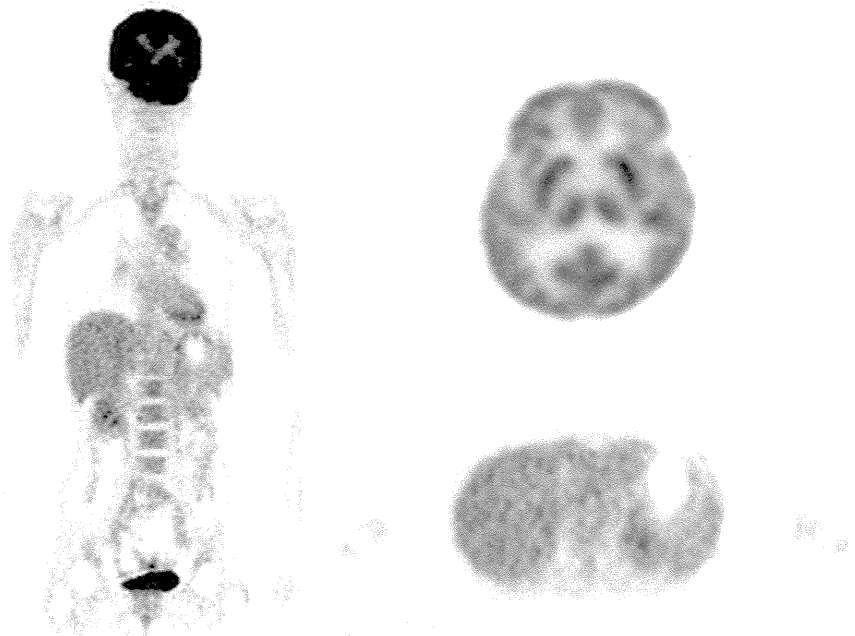**Fig. 6** NEC$_{patient}$ in 21 cases

Fig. 7 Clinical FDG-PET images (*left* coronal, *upper right* brain transverse, *lower right* liver transverse)

NEC$_{patient}$ = 33.7 (Mcounts/m), and liver SNR = 18.5 are shown in Figs. 6, 7.

Discussion

We attempted to standardize FDG-PET image quality by optimizing the scan duration and reconstruction parameters on the basis of the guideline. Phantom experiments involved determining the acquisition/reconstruction parameters by scanner model and then verifying the validity of the conditions. Centers that already had default

protocols only required the validation step. Though all of the participating centers in this trial had already performed clinical FDG-PET/CT examinations, we acquired the data for this trial using the list mode during validation in order to evaluate the data with varied acquisition durations. This procedure allowed for the simulation of PET images with varied acquisition durations, which enabled determination of optimal acquisition durations with only one phantom experiment. This was necessary when the default scanning protocol did not meet the recommendation of the guideline. However, multiple phantom experiments with varied acquisition durations

were required when utilizing PET/CT scanners with no list mode available.

With the acquisition duration that permitted visualization of the 10-mm hot sphere in the phantom experiment, the mean $NEC_{phantom}$ and N_{10mm} values were below the values recommended in the guideline while the mean $Q_{H,10mm}/N_{10mm}$ value of 2.81 was far beyond the recommended value. Visualization of a lesion depends on the correlation between image noise and contrast or $Q_{H,10mm}/N_{10mm}$. Therefore, the scanning protocol determined on the basis of the phantom experiments in this trial can guarantee sufficient image quality.

Although not included in the guideline, this trial evaluated SUV (calibration) accuracy. The Core Laboratory of the ACRIN uses a cylindrical phantom for 18F or 68Ge to evaluate the calibration accuracy within 10 % or less than 10 %. In this trial, we applied the same allowance range for calibration evaluation and determined that two scanners (10.2 %) did not meet the allowance range. Our phantom shape was different from ACRIN's but the influence should be minor. One of the two scanners required an adjustment and the other required an adjustment of the dose calibrator. Both scanners attained the acceptable accuracy after recalibration. This indicated that the phantom experiment was useful for identifying the physical error or calibration process error of the scanner.

Phantom experiments resulted in prolonged data acquisition duration in 10 centers. As of August 2012, 21 patients had undergone FDG-PET examination for this trial. The QA parameters $NEC_{patient}$, $NEC_{density}$, and liver SNR were all beyond the levels recommended in the guideline, suggesting that the accumulated image data have sufficient quality for the trial.

While there is currently (August 2012) no Core Laboratory representing the entire academic community in Japan, this trial was directed by the special Core Laboratory established for JSCT NHL10 and was facilitated by the collaboration of the Japan Society of Nuclear Medicine Working Group members (principal investigator: Ukihide Tateishi, MD., PhD).

The phantom experiments were performed based on the guideline to optimize the acquisition protocol and standardize the image quality used in the multicenter trial to assess mid-therapy FDG-PET/CT. Phantom experiments enabled accumulation of sufficient quality image data across multiple centers.

References

1. Seam P, Juweid ME, Cheson BD. The role of FDG-PET scans in patients with lymphoma. Blood. 2007;110(10):3507–16.
2. Spaepen K, Stroobants S, Dupont P, Vandenberghe P, Thomas J, de Groot T, et al. Early restaging positron emission tomography with (18)F-fluorodeoxyglucose predicts outcome in patients with aggressive non-Hodgkin's lymphoma. Ann Oncol. 2002;13(9): 1356–63.
3. Gallamini A, Rigacci L, Merli F, Nassi L, Bosi A, Capodanno I, et al. The predictive value of positron emission tomography scanning performed after two courses of standard therapy on treatment outcome in advanced stage Hodgkin's disease. Haematologica. 2006;91(4):475–81.
4. Casasnovas RO, Meignan M, Berriolo-Riedinger A, Bardet S, Julian A, Thieblemont C, et al. SUVmax reduction improves early prognosis value of interim positron emission tomography scans in diffuse large B-cell lymphoma. Blood. 2011;118(1):37–43.
5. Haioun C, Itti E, Rahmouni A, Brice P, Rain JD, Belhadj K, et al. [18F]fluoro-2-deoxy-D-glucose positron emission tomography (FDG-PET) in aggressive lymphoma: an early prognostic tool for predicting patient outcome. Blood. 2005;106(4):1376–81.
6. Kasamon YL, Wahl RL, Ziessman HA, Blackford AL, Goodman SN, Fidyk CA, et al. Phase II study of risk-adapted therapy of newly diagnosed, aggressive non-Hodgkin lymphoma based on midtreatment FDG-PET scanning. Biol Blood Marrow Transplant. 2009;15(2):242–8.
7. Pregno P, Chiappella A, Bellò M, Botto B, Ferrero S, Franceschetti S, et al. Interim 18-FDG-PET/CT failed to predict the outcome in diffuse large B-cell lymphoma patients treated at the diagnosis with rituximab-CHOP. Blood. 2012;119(9):2066–73.
8. Zijlstra JM, Boellaard R, Hoekstra OS. Interim positron emission tomography scan in multi-center studies: optimization of visual and quantitative assessments. Leuk Lymphoma. 2009;50(11): 1748–9.
9. Kurihara C. Report of the participation in the US Society of Nuclear Medicine Clinical Trial Network Summit meeting. Clin Eval. 2010;38(3):623–8.
10. Scheuermann JS, Saffer JR, Karp JS, Levering AM, Siegel BA. Qualification of PET scanners for use in multicenter cancer clinical trials: The American College of Radiology Imaging Network Experience. J Nucl Med. 2009;50(7):1187–93.
11. http://www.jsnm.org/japanese/11-12-13. Accessed 31 Jul 2012.
12. Fukukita H, Senda M, Terauchi T, Suzuki K, Daisaki H, Matsumoto K, et al. Japanese guideline for the oncology FDG-PET/CT data acquisition protocol: synopsis of Version 1.0. Ann Nucl Med. 2010;24(4):325–34.
13. National Electrical Manufacturers Association. NEMA Standards Publication NU 2-2007: performance measurement of positron emission tomographs. Rosslyn, VA: National Electrical Manufacturers Association; 2007.

Comparative study of the value of dual tracer PET/CT in evaluating breast cancer

Ukihide Tateishi,[1,7] Takashi Terauchi,[2] Sadako Akashi-Tanaka,[3] Takayuki Kinoshita,[4] Daisuke Kano,[2] Hiromitsu Daisaki,[2] Takeshi Murano,[2] Hitoshi Tsuda[5] and Homer A. Macapinlac[6]

[1]Department of Radiology, Yokohama City University Graduate School of Medicine, Kanagawa; [2]Division of Screening Technology and Development, Research Center for Cancer Prevention and Screening, National Cancer Center, Tokyo; [3]Breast Oncology, Showa University School of Medicine, Tokyo; [4]Division of Breast Surgery and [5]Pathology and Clinical Laboratory Division, National Cancer Center Hospital, Tokyo, Japan; [6]Department of Nuclear Medicine, University of Texas, MD Anderson Cancer Center, Houston, Texas, USA

The present study was conducted to assess the relationship between tumor uptake and pathologic findings using dual-tracer PET/computed tomography (CT) in patients with breast cancer. Seventy-four patients with breast cancer (mean age 54 years) who underwent ^{11}C-choline and 2-[^{18}F]fluoro-2-deoxy-D-glucose (^{18}F-FDG) PET/CT prior to surgery on the same day were enrolled in the present study. Images were reviewed by a board-certified radiologist and two nuclear medicine specialists who were unaware of any clinical information and a consensus was reached. Uptake patterns and measurements of dual tracers were compared with the pathologic findings of resected specimens as the reference standard. Mean ($\pm$SD) tumor size was 5.9 $\pm$ 3.2 cm. All primary tumors were identified on ^{18}F-FDG PET/CT and ^{11}C-choline PET/CT. However, ^{18}F-FDG PET/CT demonstrated focal uptake of the primary tumor with ($n = 38$; 51%) or without ($n = 36$; 49%) diffuse background breast uptake. Of the pathologic findings, multiple logistic regression analysis revealed an independent association between fibrocystic change and diffuse background breast uptake (odds ratio [OR] 8.57; 95% confidence interval [CI] 2.86–25.66; $P < 0.0001$). Tumors with higher histologic grade, nuclear grade, structural grade, nuclear atypia, and mitosis had significantly higher maximum standardized uptake values (SUV$_{max}$) and tumor-to-background ratios (TBR) for both tracers. Multiple logistic regression analysis revealed that only the degree of mitosis was independently associated with a high SUV$_{max}$ (OR 7.45; 95%CI 2.21–25.11; $P = 0.001$) and a high TBR (OR 5.41; 95%CI 1.13–25.96; $P = 0.035$) of ^{11}C-choline PET/CT. In conclusion, ^{11}C-choline may improve tumor delineation and reflect tumor aggressiveness on PET/CT in patients with breast cancer. (*Cancer Sci* 2012; 103: 1701–1707)

Positron emission tomography/computed tomography (PET/CT) with the glucose analog 2-[^{18}F]fluoro-2-deoxy-D-glucose (^{18}F-FDG) is recognized as an important tool in initial tumor evaluation, including staging, in the evaluation of treatment response, and in the assessment of recurrent disease for breast cancer.[1,2] It has been reported that PET/CT adds incremental diagnostic confidence to PET in 60% of patients and in >50% of regions with increased ^{18}F-FDG uptake.[3] Tatsumi *et al.*[4] concluded that PET/CT was preferable in evaluating breast cancer lesions in view of the level of diagnostic confidence that it allows. Regardless of the exact type of PET/CT fusion technique, ^{18}F-FDG uptake in non-malignant conditions often leads to high background uptake on breast imaging.[5]

Histological changes are the cause of considerable variations and false-positive findings on breast imaging. Fibrocystic changes (FCC) are the most common of these conditions that can affect the assessment of imaging features on mammography[6,7] and MRI.[8,9] Similarly, there is evidence in the literature that ^{18}F-FDG PET and accelerated glucose metabolism as

a result of FCC lead to false-positive findings and difficulty in determining the boundary of specificity.[10]

Choline is an essential component of the cell membrane and choline uptake is upregulated by choline kinase-α, which catalyses the phosphorylation of choline.[11,12] In mammary epithelial cells, levels of phosphocholine metabolites increase due to overexpression of choline kinase-α, which is regulated by the mitogen-activated protein kinase (MAPK) pathway.[11–13] Recent clinical studies in patients with breast carcinoma undergoing molecular-targeted therapy suggest that ^{11}C-choline uptake is 10-fold higher in aggressive breast carcinoma phenotypes and that the uptake of ^{11}C-choline on PET is correlated with tumor grade.[13] Thus, ^{11}C-choline is considered a promising radiotracer for the evaluation of breast cancer in the clinical setting prior to treatment.

Although both data from ^{18}F-FDG and ^{11}C-choline PET/CT allow more precise evaluation of the primary breast cancer, direct comparisons of these two tracers in breast cancer have not been made. In the present study, we sought to confirm and extend previous findings of ^{11}C-choline PET/CT studies by investigating the association between histological findings and the results of ^{18}F-FDG PET/CT investigations in patients with breast cancer.

Materials and Methods

Patients. Seventy-four patients (mean age 54 years; range 25–89 years) with breast carcinoma were enrolled in the present retrospective dual PET/CT study between March 2008 and March 2010. Patients were eligible for inclusion in the study if they met the following criteria: (i) performance status 0 or 1; (ii) no concomitant malignancy; (iii) histologically proven breast carcinoma diagnosed by biopsy at least 1 month before; and (iv) no history of hormone therapy. All patients were required to provide written informed consent. A regimen of 5-fluorouracil, epirubicin, and cyclophosphamide (FEC) plus paclitaxel was used as neoadjuvant chemotherapy in 32 patients (43%). As a rule, hormone therapy was introduced after completion of imaging studies if needed. Our institutional review board (National Cancer Center Hospital, Tokyo, Japan) approved the present study, which complied with the Health Insurance Portability and Accountability Act. The clinical records of all patients were available for review. All patients received surgery after imaging studies.

Phantom study. A phantom study of PET/CT was performed prior to the clinical study at two institutions to clarify the optimum conditions for data acquisition and to ensure quality control.[14] Studies were performed with a whole-body PET/CT

scanner (Aquiduo PCA-7000B; Toshiba Medical Systems, Tochigi, Japan). The CT component of the scanner has a 16-row detector. We used an NEMA image quality (IQ) phantom (NU 2-2001) for cross calibration, because this type of phantom is used in many institutions and data regarding the estimation of the optimum time are available. The radioactivity concentration of the background was set at 2.6 ± 0.2 kBq/mL ^{18}F-FDG, similar to that in clinical settings. The radioactivity concentration of the hot portion was fourfold greater than that of the background. Data were collected over a period of 2–5 min in the dynamic acquisition mode and for 30 min in the static acquisition mode. The data acquired, including normalization data, cross-calibration data, blank scan data, and transmission data, were assessed for visual inspection, phantom noise equivalent count ($NEC_{phantom}$), percentage contrast ($Q_{H,10\ mm}$) and percentage background variability ($N_{10\ mm}$). The preferred parameters pertinent to the clinical condition were $NEC_{phantom} > 10.4$ (counts), $N_{10\ mm} < 6.2\%$, and $Q_{H10\ mm}/N_{10\ mm} > 1.9\%$. After a review of the data analyses, the optimum conditions for the PET/CT were determined as follows: data acquisition, 180 s for one bed; field-of-view, 500 mm; iteration, 4; subset, 14; matrix size,128 × 128; filter, Gaussian 8 mm in full width at half maximum; reconstruction, ordered-subsets expectation maximization (OSEM).

Data acquisition. ^{11}C-Choline was synthesized using a commercially available module, as described by Hara *et al.*[15] Prior to the ^{11}C-choline PET/CT study, patients fasted for at least 6 h. Immediately after they had evacuated their bladder, patients were placed in a supine, arm-up position. For the PET/CT, low-dose CT data were first acquired at 120 kVp using an autoexposure control system (beam pitch 0.875 or 1 and 1.5 or 2 mm × 16-row mode). Data acquisition was performed for each patient from the top of the skull to the mid-thigh. Patients maintained normal shallow respiration during the three-dimensional acquisition of CT scans. No iodinated contrast material was administered. Acquisition of emission scans from the head to the mid-thigh was started 5 min after intravenous administration of a mean ^{11}C-choline dose of 475 MBq (range 469–491 MBq). The ^{18}F-FDG PET/CT study was performed 1 h after the ^{11}C-choline PET/CT study in all patients. Patients received an intravenous injection of 311 MBq (range 197–397 MBq) ^{18}F-FDG with an uptake phase at 64 ± 5 min.

Image interpretation. Dedicated software (Vox-base SP1000 workstation; J-MAC Systems, Sapporo, Japan) was used to review all PET, CT, and coregistered PET/CT images in all standard planes. Images were analyzed visually and quantitatively by two independent reviewers, who recorded their findings after reaching a consensus. A region of interest (ROI) was outlined within areas of increased uptake and measured on each slice. When the lesion was extensively heterogeneous, the ROI was set so as to cover all the components of the lesion. The diffuse pattern of breast was assigned to the breast that shows homogeneous accumulation greater than aortic blood except for the primary lesion. For quantitative interpretations, the standardized uptake value (SUV) was determined according to the standard formula, with activity in the ROI recorded as Bq/mL per injected dose (Bq) per weight (kg), but time decay correction for whole-body image acquisition was not performed. The maximum SUV (SUV_{max}) was recorded using the maximum pixel activity within the ROI. The tumor-to-background ratio (TBR) was calculated with reference to uptake in the contralateral breast.

Pathologic analysis. All patients underwent surgery. Each tumor was staged according to the TNM classification of the International Union against Cancer.[16] Resected specimens were fixed in 10% buffered formalin and embedded in paraffin wax. Then, 4-μm sections were obtained in a plane perpendic-

ular to the long axis of the breast. Paraffin-embedded microslices were stained with H&E. Tissue grading, nuclear grading, and structural grading were done using the grading system of Elston and Ellis.[17] Estrogen receptor (ER) and progesterone receptor status was evaluated using the H-scoring system of McCarty *et al.*[18] Human epidermal growth factor-2 (HER-2/neu) was evaluated by immunostaining with 4B5 primary antibody. Evaluation of the primary lesion was based on the following pathologic findings: FCC, differentiation, subtype, location, diameter of the invasive component, diameter of the non-invasive component, ratio of the invasive component in the tumor (%), tissue grading, nuclear grading, structural grading, nuclear atypia, mitosis, necrosis, fat invasion, cutaneous invasion, muscular invasion, ER status, progesterone receptor status, and HER-2/neu status. In the present study, "non-invasive component" referred to ductal carcinoma *in situ* (DCIS).

Statistical analysis. The Chi-squared test or Fisher's exact probability test were used to compare pathologic findings associated with PET/CT findings. In addition, the Wald test and 95% confidence intervals (CI) were used to evaluate the statistical significance of individual variables. To determine relationships of SUV and TBR between the two tracers, we used Spearman rank correlation. Comparisons of mean values between groups were made using Student's *t*-test or analysis of variance (ANOVA) with Bonferroni's adjustment for multiple comparisons. Parsimonious univariate and multivariate logistic regression models were used to measure independent associations with PET/CT findings. Statistical tests used a two-sided significance level of 0.05. Statistical analyses were performed using PASW Statistics 19 (IBM, Tokyo, Japan).

Results

In all, 74 patients completed the study procedures. The demographic data for all patients are given in Table 1. There were 66 patients (89%) with invasive tumors, 60 of which were ductal carcinoma and six lobar carcinoma. Eight patients (11%) had non-invasive ductal carcinoma.

All primary tumors were identified on ^{18}F-FDG PET/CT and ^{11}C-choline PET/CT (Fig. 1). The SUV_{max} of ^{11}C-choline PET/CT was significantly lower than that of ^{18}F-FDG PET/CT ($P = 0.002$; Table 2). Conversely, the TBR of ^{11}C-choline PET/CT was significantly higher than that of ^{18}F-FDG PET/CT ($P < 0.0001$; Table 2). Using ^{18}F-FDG PET/CT, focal uptake of the primary tumor with ($n = 38$ [51%]; Fig. 2) or without ($n = 36$ [49%]) diffuse background breast uptake was demonstrated. Conversely, ^{11}C-choline PET/CT showed only focal uptake of the primary tumor in all patients. There were

Table 1. Patient demographics

Age (years)	54 ± 13 (24–78)
Tumor side	
Right	44 (59)
Left	30 (41)
Tumor size (cm)	5.9 ± 3.2 (1.8–12.0)
Main location	
Medial upper quadrant	8 (11)
Medial lower quadrant	8 (11)
Lateral upper quadrant	46 (62)
Lateral lower quadrant	6 (8)
Central	2 (3)
Invasive tumor	66 (89)
Non-invasive tumor	8 (11)

Data are given as the mean ± SD, with the range in parentheses, or as the number of patients in each group with percentages in parentheses.
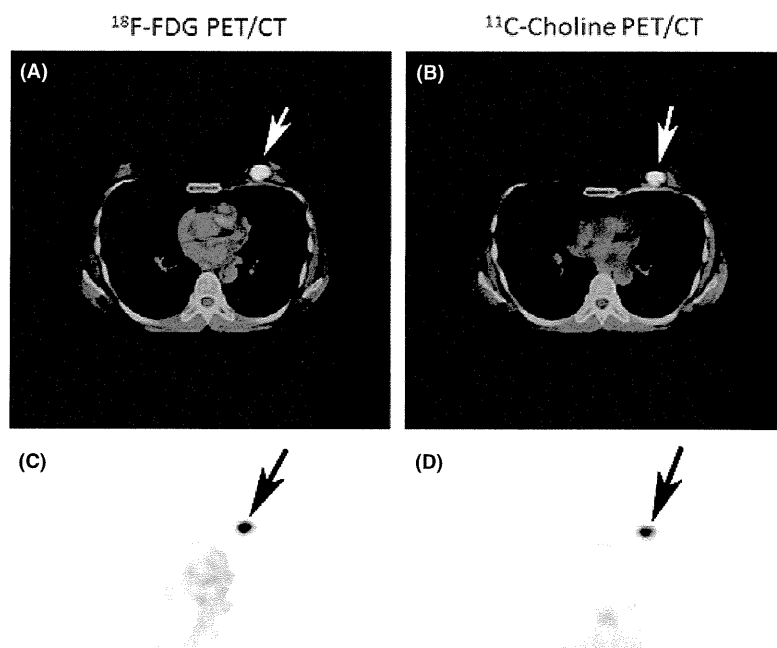
1702

Fig. 1. Results for a 51-year-old woman with invasive ductal carcinoma of the left breast. (a,c) ^{18}F-fludeoxyglucose (FDG) PET/computed tomography (CT) images (fusion image: a; PET alone: (c) reveal a focal hypermetabolic focus in the primary tumor (arrows). The maximum standardized uptake value (SUV$_{max}$) was 5.5 and the tumor-to-background ratio (TBR) was 47.0. (b,d) Transverse ^{11}C-choline PET/CT images (fusion image: b; PET alone: d) also reveal a focal hypermetabolic focus in the primary tumor (arrows). The SUV$_{max}$ was 5.0 and the TBR was 137.5. On microscopy, the tumor contained 100% invasive component.

Table 2. Computed tomography (CT)/PET measurements and pathologic components with or without diffuse background breast uptake on ^{18}F-fludeoxyglucose PET/CT

	Total	With diffuse uptake	Without diffuse uptake	P-value
^{11}C-Choline uptake of tumor				
SUV$_{max}$ (g/mL)	3.7 ± 2.9	3.6 ± 3.5	3.8 ± 2.0	0.789
TBR	8.0 ± 6.0	7.7 ± 9.9	8.3 ± 9.8	0.709
^{18}F-FDG uptake of tumor				
SUV$_{max}$ (g/mL)	4.4 ± 3.1	4.6 ± 3.6	4.2 ± 2.5	0.571
TBR	3.7 ± 2.7	3.2 ± 2.4	4.5 ± 2.9	0.016
Diameter of invasive tumor (cm)	4.1 ± 3.5	4.2 ± 4.0	4.0 ± 3.0	0.800
Diameter of non-invasive tumor (cm)	1.8 ± 2.3	2.6 ± 2.9	0.9 ± 1.0	0.002
% Invasive component	66.0 ± 36.5	54.0 ± 41.4	78.6 ± 25.4	0.003

FDG, fludeoxyglucose; SUV$_{max}$, maximum standardized uptake value; TBR, tumor-to-background ratio.

significant differences between patients with or without diffuse background breast uptake on ^{18}F-FDG PET/CT for TBR of ^{18}F-FDG (Table 2). There was no interaction between ^{11}C-choline uptake and background breast uptake patterns on ^{18}F-FDG PET/CT. There were significant differences for the diameter of the non-invasive component and the percentage invasive component between patients with and without diffuse background breast uptake on ^{18}F-FDG PET/CT (Table 2).

The pathologic findings and background breast uptake patterns on ^{18}F-FDG PET/CT are listed in Table 3. Patients with

diffuse background breast uptake had significantly different values for percentage invasive component, FCC, necrosis, and triple negative tumor compared with patients without diffuse background breast uptake. There were no significant differences between the two groups in histologic grade, nuclear grade, structural grade, nuclear atypia, mitosis, fat invasion, or cutaneous invasion. Nor were there any significant differences in hormone receptor status between the two groups, specifically HER-2/neu, ER, and progesterone receptors. Only FCC showed an independent association with diffuse background breast uptake on multiple logistic regression analysis (OR 8.57; 95% CI 2.86–25.66; P < 0.0001).

There was a modest correlation between the diameter of the invasive tumor and SUV$_{max}$ (P < 0.0001) or TBR (P = 0.006) on ^{18}F-FDG PET/CT (Table 4). Similar trends were found between the diameter of the invasive tumor and SUV$_{max}$ (P < 0.0001) and TBR (P < 0.0001) on ^{11}C-choline PET/CT (Table 5). The TBR on ^{11}C-choline PET/CT also showed a modest correlation with the percentage invasive component (P = 0.047). The diameter of the non-invasive tumor was not correlated with SUV$_{max}$ or TBR on either ^{18}F-FDG or ^{11}C-choline PET/CT.

Pathologic characteristics and tracer uptake are summarized in Table 6. Tumors with a higher histologic grade, nuclear grade, structural grade, nuclear atypia, and mitosis showed significantly higher SUV$_{max}$ and TBR for both ^{18}F-FDG and ^{11}C-choline PET/CT. Tumors without expression of hormone receptors, including ER and progesterone receptors, and triple negative tumors showed significantly higher SUV$_{max}$ and TBR for both ^{18}F-FDG and ^{11}C-choline PET/CT. Tumors expressing FCC and fat invasion were more likely to have high SUV$_{max}$ and TBR on ^{11}C-choline PET/CT, but these differences were not identified in the TBR of ^{18}F-FDG PET/CT. In addition, tumors with necrosis and cutaneous invasion were found to have greater SUV$_{max}$ and TBR only on ^{11}C-choline PET/CT. There was no significant association between the SUV$_{max}$ or TBR and the percentage of invasive component or the HER-2/neu status for both tracers. After adjusting for age and tumor size, multiple logistic regression analysis revealed that the degree of mitosis was independently associated with high
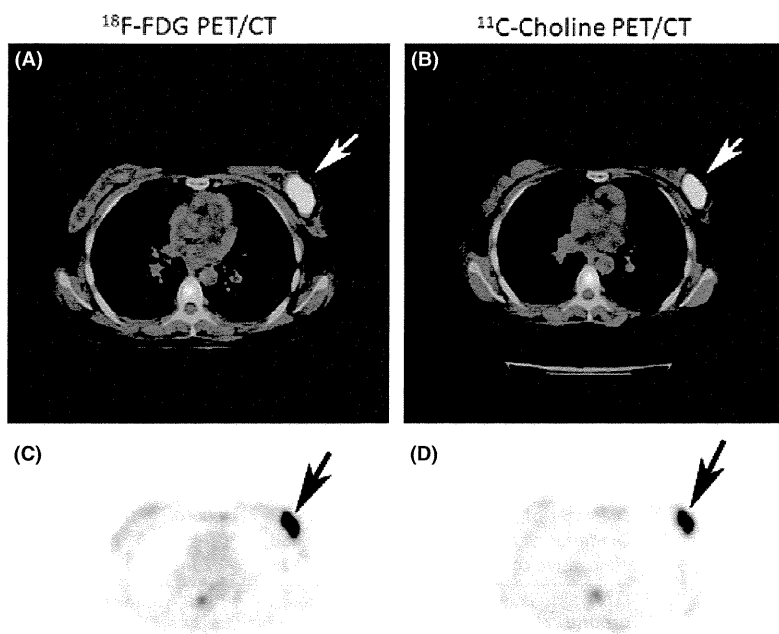
^{18}F-FDG PET/CT ^{11}C-Choline PET/CT

(A)   (B)

(C)   (D)

Fig. 2. Results for a 47-year-old woman with invasive scirrhous carcinoma of the left breast. (a,c) ^{18}F-fludeoxyglucose (FDG) PET/computed tomography (CT) images (fusion image: a; PET alone: c) reveal a focal hypermetabolic focus (arrows) of the primary tumor with diffuse background breast uptake. The maximum standardized uptake value (SUV$_{max}$) was 5.4 and the tumor-to-background ratio (TBR) was 35.7. (b,d) Transverse ^{11}C-choline PET/CT images (fusion image: b; PET alone: (d) reveal only a focal hypermetabolic focus in the primary tumor (arrows). The SUV$_{max}$ was 5.0 and the TBR was 125.0. On microscopy, the tumor contained 15% invasive component. Diffuse fibrocystic changes were found in the background breast.

SUV$_{max}$ (OR 7.45; 95% CI 2.21–25.11; P = 0.001) and high TBR (OR 5.41; 95% CI; 1.13–25.96; P = 0.035) of ^{11}C-choline PET/CT.

Discussion

The present study examined the association between dual-tracer uptake and histological background in breast cancer. Despite positive correlations for SUV$_{max}$ or TBR with ^{18}F-FDG and ^{11}C-choline, mitosis was found to be correlated with ^{11}C-choline uptake only, which reflects tumor aggressiveness reported in the previous study of patients with breast cancer.[19] The results also reveal that diffuse background breast uptake on ^{18}F-FDG PET/CT depends on FCC and this pattern of uptake was not identified in any patients on ^{11}C-choline PET/CT. Our findings suggest that ^{11}C-choline may be feasible for the imaging of breast cancer particularly for patients with underlying FCC in whom mammography and ^{18}F-FDG PET/CT are limited.

Our observation of a positive correlation between mitosis and ^{11}C-choline uptake supports results reported in previous studies.[13,19] This phenomenon was not affected by the underlying histological background because comparative correlation coefficients of SUV$_{max}$ and TBR were similar on ^{11}C-choline PET/CT. Furthermore, the association between mitosis and ^{18}F-FDG uptake was not observed, regardless of positive correlation between ^{18}F-FDG and ^{11}C-choline uptake. This discrepancy in terms of mitosis and tracer uptake in our patients is presumably caused by differences in the degree of tracer uptake.

The present study demonstrated that there were significant differences in the diameter of the non-invasive component and the percentage invasive component between patients with and without diffuse background breast uptake on ^{18}F-FDG PET/CT. However, the SUV$_{max}$ and TBR of both tracers were similar between patients with or without diffuse background breast uptake on ^{18}F-FDG PET/CT. These results suggest that the non-invasive component of breast cancer, which refers to the DCIS component in the present study, cannot be depicted by both tracers. These findings are consistent with that of another study that suggested DCIS could not be precisely visualized by PET.[1] Neubauer et al.[20] suggested that the DCIS component

could be detected by dynamic contrast-enhanced MRI, but the specificity was unfavorable because of an overlap in kinetic curve appearance. A major limitation of previous studies, as well as the present study, is that whole-body PET/CT scanners were used to evaluate primary lesion of the breast.

Fibrocystic changes are the most common diffuse benign condition of the breast related to changes in responses to estrogen and progesterone. The histology of FCC varies considerably and includes cysts, apocrine metaplasia, fibrosis, calcification, ductal hyperplasia, adenosis, and fibroadenomatous changes.[21,22] Because of its diverse appearances and kinetic features, FCC is major cause of false-positive findings on MRI.[23–25] As for PET studies, Yutani et al.[26] have previously explored the ^{18}F-FDG uptake of FCC in 38 patients with breast cancer, providing evidence that diffuse ^{18}F-FDG uptake caused by accompanying FCC obscures uptake by the primary tumor. Palmedo et al.[27] have confirmed that FCC is a major cause of reduced specificity in the detection of primary breast cancers on ^{18}F-FDG PET. Furthermore, Kole et al.[28] compared the detectability of primary lesions between ^{18}F-FDG PET and ^{11}C-tyrosine PET in patients with breast cancer and concluded that the visual assessment and delineation of the primary tumor were complicated only on ^{18}F-FDG PET when the contralateral breast tissue served as the control because FCC is a bilateral disease. As far as we were aware, the present study is the first that has been designed to evaluate the primary lesion of breast cancer using the dual tracers of ^{18}FDG and ^{11}C-choline. However, considering the high incidence of FCC, PET tracers including ^{11}C-tyrosine and ^{11}C-choline in addition to ^{18}F-FDG are more likely to fulfill specificity expectations.

The exact mechanism of ^{11}C-choline uptake by tumor cells is largely unknown; however, ^{11}C-choline has been proposed as a marker of the extracellular receptor kinase/MAPK pathway, exhibits significant uptake in tumor tissues, and is regarded as a favorable tracer for breast cancer.[13] ^{11}C-Choline uptake may occur via a choline-specific transporter protein that is overexpressed in the cell membranes of breast cancer. ^{11}C-Choline is phosphorylated by choline kinase, which is upregulated in tumor cells for the synthesis of phosphatidylcholine, and is retained within tumor cells.[11,12] Phosphatidylcholine is an essential

Table 3. Pathologic characteristics and background breast uptake on ^{18}F-fludeoxyglucose PET/computed tomography

	No. patients		P-value
	With diffuse uptake	Without diffuse uptake	
Invasive component			
>30%	20	32	0.001
<30%	18	4	
Fibrocystic change			
Present	24	6	<0.0001
Absent	14	30	
Histologic grade			
1 or 2	16	22	0.102
3	22	14	
Nuclear grade			
1 or 2	16	22	0.102
3	22	14	
Structural grade			
1 or 2	14	18	0.253
3	24	18	
Nuclear atypia			
1 or 2	16	20	0.247
3	22	16	
Mitosis			
1 or 2	26	20	0.254
3	12	16	
Necrosis			
Present	22	8	0.002
Absent	16	28	
Fat invasion			
Present	22	24	0.437
Absent	16	12	
Cutaneous invasion			
Present	4	4	0.163
Absent	32	32	
HER-2/neu receptor			
Positive	22	14	0.102
Negative	16	22	
Estrogen receptor			
Positive	28	21	0.163
Negative	10	15	
Progesterone receptor			
Positive	28	21	0.163
Negative	10	15	
Triple negative			
Yes	4	11	0.032
No	34	25	

Table 4. Relationship between ^{18}F-fludeoxyglucose uptake and invasive or non-invasive tumor components

	^{18}F-FDG			
	SUV_{max}	P-value	TBR	P-value
Diameter of invasive tumor	0.381	<0.0001	0.318	0.006
Diameter of non-invasive tumor	-0.058	0.625	-0.14	0.234
% Invasive component	0.126	0.286	0.189	0.089

FDG, fludeoxyglucose; SUV_{max}, maximum standardized uptake value; TBR, tumor-to-background ratio.

Table 5. Relationship between ^{11}C-choline uptake and invasive or non-invasive tumor components

	^{11}C-Choline			
	SUV_{max}	P-value	TBR	P-value
Diameter of invasive tumor	0.425	<0.0001	0.537	<0.0001
Diameter of non-invasive tumor	0.038	0.745	-0.066	0.575
% Invasive component	0.125	0.29	0.232	0.047

SUV_{max}, maximum standardized uptake value; TBR, tumor-to-background ratio.

component of cell membranes and is involved in the modulation of transmembrane signaling by carcinogenesis. Therefore, ^{11}C-choline metabolism is accelerated in cell proliferation and is enhanced with increasing tumor grade of breast cancer. In the present study, tumors with higher histologic grade, nuclear grade, structural grade, nuclear atypia, and mitosis showed significantly higher SUV_{max} and TBR for ^{11}C-choline PET/CT. These results are in accord with those of previous *in vivo* and *in vitro* studies.[19,29]

^{11}C-Choline PET/CT has been introduced as feasible method for the evaluation of breast cancer. In the present study, tumors without ER or progesterone receptors and triple negative tumors showed greater uptake of ^{11}C-choline compared with control groups. This suggests that ^{11}C-choline uptake reflects tumor aggressiveness. In a study of 32 patients with pathologically proven breast cancer expressing ER, no association was found between ^{11}C-choline uptake and hormone

receptor status.[19] The apparent discrepancy between the present study and those of the previous study[19] may be due, in large part, to differences in the patient populations studied.

In the present study, tumors exhibiting fat invasion were more likely to have a high SUV_{max} and TBR on ^{11}C-choline PET/CT, but these differences were not identified in the TBR of ^{18}F-FDG PET/CT. This appeared to be associated with diffuse ^{18}FDG uptake of breast caused by accompanying FCC, which may obscure tumor delineation. The presence of necrosis or cutaneous invasion was also found to have an association with SUV_{max} and TBR on ^{11}C-choline PET/CT. Overall, our results are consistent with those reported in *in vivo* and *in vitro* studies, in which ^{11}C-choline uptake was found to reflect tumor aggressiveness of breast cancer.[13,19]

The present study design had limitations. First, the present study was designed to assess tumor uptake of dual tracers prior to surgery. The results from a breast cancer patient population of will not fully explain the detectability of advanced or recurrent disease. Second, the present study was an observational study and not a clinical trial, which raises the possibility of confounding factors affecting the results. Third, although ^{11}C-choline is clearly a possible PET tracer for tumor localization in patients with breast cancer, its short half-life restricts its practical application. However, ^{18}F-choline is a tracer with a longer half-life than that of ^{11}C-choline, and so ^{18}F-choline may improve the accuracy of tumor localization. Additional comparative studies regarding detectability and pathologic correlation are needed to validate the findings of the present study. Although we found that ^{11}C-choline uptake reflected tumor aggressiveness in patients with breast cancer, we did not have any data regarding nodal status and follow-up management of the patients. Further studies are needed to clarify the relationship between ^{11}C-choline uptake and patient outcome with a long follow-up period.

In conclusion, the results of the present study suggest that ^{11}C-choline PET/CT allows for the evaluation of tumor aggressiveness and improves delineation of primary tumors compared with ^{18}F-FDG PET/CT in patients with breast cancer. The results demonstrate the advantages and potential of ^{11}C-choline, but clinical evaluation with a long follow-up

Table 6. Pathologic characteristics and tracer uptake

	^{11}C-Choline				^{18}F-FDG			
	SUV$_{max}$	P-value	TBR	P-value	SUV$_{max}$	P-value	TBR	P-value
% Invasive component		0.979		0.432		0.934		0.79
>30%	3.7 ± 2.3		8.5 ± 5.6		4.4 ± 3.1		3.9 ± 2.4	
<30%	3.7 ± 3.5		7.4 ± 6.4		4.4 ± 3.1		4.1 ± 3.2	
Fibrocystic change		<0.0001		<0.0001		0.002		0.429
Present	5.4 ± 3.5		11.4 ± 6.7		5.7 ± 3.5		4.3 ± 2.2	
Absent	2.5 ± 1.6		5.7 ± 4.0		3.5 ± 2.5		3.8 ± 3.1	
Histologic grade		<0.0001		<0.0001		<0.0001		<0.0001
1 or 2	2.2 ± 1.1		4.4 ± 2.5		2.9 ± 2.0		2.9 ± 2.3	
3	5.3 ± 3.3		11.8 ± 6.2		6.1 ± 3.3		5.2 ± 2.8	
Nuclear grade		<0.0001		<0.0001		<0.0001		<0.0001
1 or 2	2.2 ± 1.1		4.4 ± 2.5		2.9 ± 2.0		2.9 ± 2.3	
3	5.3 ± 3.3		11.8 ± 6.2		6.1 ± 3.3		5.2 ± 2.8	
Structural grade		<0.0001		<0.0001		<0.0001		0.011
1 or 2	2.3 ± 1.5		4.7 ± 3.5		3.0 ± 2.4		3.1 ± 2.7	
3	4.8 ± 3.2		10.5 ± 6.3		5.5 ± 3.2		4.7 ± 2.7	
Nuclear atypia		<0.0001		<0.0001		<0.0001		0.012
1 or 2	2.1 ± 1.1		4.2 ± 2.4		2.8 ± 2.0		2.8 ± 2.3	
3	5.2 ± 3.3		11.6 ± 6.1		5.9 ± 3.2		5.1 ± 2.7	
Mitosis		<0.0001		<0.0001		<0.0001		<0.0001
1 or 2	2.1 ± 1.1		4.5 ± 2.5		2.8 ± 1.8		2.6 ± 2.1	
3	6.4 ± 3.0		13.8 ± 5.5		7.1 ± 3.0		6.3 ± 2.1	
Necrosis		0.046		0.001		0.051		0.529
Present	4.5 ± 3.2		10.6 ± 7.1		5.3 ± 3.3		4.2 ± 2.6	
Absent	3.1 ± 2.6		6.2 ± 4.3		3.8 ± 2.9		3.8 ± 2.9	
Fat invasion		0.003		0.002		0.024		0.061
Present	4.5 ± 3.3		9.6 ± 6.5		5.0 ± 3.4		4.4 ± 2.8	
Absent	2.4 ± 1.5		5.3 ± 3.6		3.4 ± 2.2		3.2 ± 2.6	
Cutaneous invasion		0.004		<0.0001		0.133		0.706
Present	6.4 ± 3.1		14.8 ± 7.3		6.0 ± 4.7		4.3 ± 2.2	
Absent	3.4 ± 2.7		7.2 ± 5.3		4.2 ± 2.8		3.9 ± 2.8	
HER-2/neu receptor		0.53		0.772		0.518		0.766
Positive	3.5 ± 2.6		8.2 ± 6.0		4.2 ± 2.7		4.1 ± 3.1	
Negative	3.9 ± 3.2		7.8 ± 6.0		4.7 ± 3.5		3.9 ± 2.5	
Estrogen receptor		<0.0001		<0.0001		<0.0001		<0.0001
Positive	2.3 ± 1.4		5.4 ± 3.4		3.1 ± 1.8		2.9 ± 2.9	
Negative	6.3 ± 3.3		13.1 ± 6.6		7.0 ± 3.5		6.1 ± 2.5	
Progesterone receptor		<0.0001		<0.0001		<0.0001		<0.0001
Positive	2.4 ± 1.5		5.6 ± 3.7		3.1 ± 1.9		2.9 ± 2.9	
Negative	6.2 ± 3.4		12.7 ± 6.8		7.0 ± 3.5		6.1 ± 2.5	
Triple negative		<0.001		<0.0001		<0.0001		0.002
Yes	6.7 ± 3.3		12.9 ± 6.5		7.4 ± 3.8		6.2 ± 2.1	
No	2.9 ± 2.2		6.7 ± 5.2		3.7 ± 2.4		3.4 ± 2.7	

FDG, fludeoxyglucose; SUV$_{max}$, maximum standardized uptake value; TBR, tumor-to-background ratio.

period is warranted to clarify the exact role of this technique and how it affects patient outcome.

Acknowledgments

Disclosure Statement

The authors declare that they have no conflicts of interest.

Abbreviations

CT	computed tomography
DCIS	ductal carcinoma *in situ*
ER	estrogen receptor
FCC	fibrocystic change
^{18}F-FDG2-[^{18}F]	fluoro-2-deoxy-D-glucose
HER-2/neu	human epidermal growth factor-2
MAPK	mitogen-activated protein kinase
SUV$_{max}$	maximum standardized uptake value
TBR	tumor-to-background ratio

References

1 Nieweg OE, Kim EE, Wong WH *et al.* Positron emission tomography with fluorine-18-deoxyglucose in the detection and staging of breast cancer. *Cancer* 1993; **71**: 3920–5.

2 Rosen EL, Eubank WB, Mankoff DA. FDG PET, PET/CT, and breast cancer imaging. *Radiographics* 2007; **27**: S215–29.

3 Mahner S, Schirrmacher S, Brenner W *et al.* Comparison between positron emission tomography using 2-[fluorine-18]fluoro-2-deoxy-D-glucose, conven-

tional imaging and computed tomography for staging of breast cancer. *Ann Oncol* 2008; **19**: 1249–54.

4 Tatsumi M, Cohade C, Mourtzikos KA, Fishman EK, Wahl RL. Initial experience with FDG-PET/CT in the evaluation of breast cancer. *Eur J Nucl Med Mol Imaging* 2006; **33**: 254–62.

5 Lim HS, Yoon W, Chung TW *et al.* FDG PET/CT for the detection and evaluation of breast diseases: usefulness and limitations. *Radiographics* 2007; **27**: S197–213.

6 Pisano ED, Johnston RE, Chapman D *et al.* Human breast cancer specimens: diffraction-enhanced imaging with histologic correlation. Improved conspicuity of lesion detail compared with digital radiography. *Radiology* 2000; **214**: 895–901.

7 Venta LA, Wiley EL, Gabriel H, Adler YT. Imaging features of focal breast fibrosis: mammographic–pathologic correlation of noncalcified breast lesions. *AJR Am J Roentgenol* 1999; **173**: 309–16.

8 Chen JH, Liu H, Baek HM, Nalcioglu O, Su MY. Magnetic resonance imaging features of fibrocystic change of the breast. *Magn Reson Imaging* 2008; **26**: 1207–14.

9 van den Bosch MA, Daniel BL, Mariano MN *et al.* Magnetic resonance imaging characteristics of fibrocystic change of the breast. *Invest Radiol* 2005; **40**: 436–41.

10 Yutani K, Shiba E, Kusuoka H *et al.* Comparison of FDG-PET with MIBI-SPECT in the detection of breast cancer and axillary lymph node metastasis. *J Comput Assist Tomogr* 2000; **24**: 274–80.

11 Ishidate K. Choline/ethanolamine kinase from mammalian tissues. *Biochim Biophys Acta* 1997; **1348**: 70–8.

12 Uchida T, Yamashita S. Molecular cloning, characterization, and expression in *Escherichia coli* of a cDNA encoding mammalian choline kinase. *J Biol Chem* 1992; **267**: 10156–62.

13 Kenny LM, Contractor KB, Hinz R *et al.* Reproducibility of [11C]choline-positron emission tomography and effect of trastuzumab. *Clin Cancer Res* 2010; **16**: 4236–45.

14 Fukukita H, Senda M, Terauchi T *et al.* Japanese guideline for the oncology FDG-PET/CT data acquisition protocol: synopsis of Version 1.0. *Ann Nucl Med* 2010; **24**: 325–34.

15 Hara T, Yuasa M. Automated synthesis of [11C]choline, a positron-emitting tracer for tumor imaging. *Appl Radiat Isot* 1999; **50**: 531–3.

16 Sobin LH, Wittekind C. *UICC TNM Classification of Malignant Tumours*, 6th edn. New York: Wiley, 2002.

17 Elston CW, Ellis IO. Pathological prognostic factors in breast cancer. I. The value of histological grade in breast cancer: experience from a large study with long-term follow-up. *Histopathology* 2002; **41**: 154–61.

18 McCarty KS Jr, Szabo E, Flowers JL *et al.* Use of a monoclonal anti-estrogen receptor antibody in the immunohistochemical evaluation of human tumors. *Cancer Res* 1986; **46**: s4244–8.

19 Contractor KB, Kenny LM, Stebbing J *et al.* [11C]choline positron emission tomography in estrogen receptor-positive breast cancer. *Clin Cancer Res* 2009; **15**: 5503–10.

20 Neubauer H, Li M, Kuehne-Held R, Schneider A, Kaiser WA. High grade and non-high grade ductal carcinoma *in situ* on dynamic MR mammography: characteristic findings for signal increase and morphological pattern of enhancement. *Br J Radiol* 2003; **76**: 3–12.

21 Guinebretière JM, Lê Monique G, Gavoille A, Bahi J, Contesso G. Angiogenesis and risk of breast cancer in women with fibrocystic disease. *J Natl Cancer Inst* 1994; **86**: 635–6.

22 Bodian CA, Perzin KH, Lattes R, Hoffmann P. Reproducibility and validity of pathologic classifications of benign breast disease and implications for clinical applications. *Cancer* 1993; **71**: 3908–13.

23 Revelon G, Sherman ME, Gatewood OM, Brem RF. Focal fibrosis of the breast: imaging characteristics and histopathologic correlation. *Radiology* 2000; **216**: 255–9.

24 Orel SG, Schnall MD, LiVolsi VA, Troupin RH. Suspicious breast lesions: MR imaging with radiologic–pathologic correlation. *Radiology* 1994; **190**: 485–93.

25 Fobben ES, Rubin CZ, Kalisher L, Dembner AG, Seltzer MH, Santoro EJ. Breast MR imaging with commercially available techniques: radiologic–pathologic correlation. *Radiology* 1995; **196**: 143–52.

26 Yutani K, Tatsumi M, Uehara T, Nishimura T. Effect of patients being prone during FDG PET for the diagnosis of breast cancer. *AJR Am J Roentgenol* 1999; **173**: 1337–9.

27 Palmedo H, Bender H, Grünwald F *et al.* Comparison of fluorine-18 fluoro-deoxyglucose positron emission tomography and technetium-99*m* methoxyisobutylisonitrile scintimammography in the detection of breast tumours. *Eur J Nucl Med* 1997; **24**: 1138–45.

28 Kole AC, Nieweg OE, Pruim J *et al.* Standardized uptake value and quantification of metabolism for breast cancer imaging with FDG and l-[1–11C]tyrosine. *J Nucl Med* 1997; **38**: 692–6.

29 Yoshimoto M, Waki A, Obata A, Furukawa T, Yonekura Y, Fujibayashi Y. Radiolabeled choline as a proliferation marker: comparison with radiolabeled acetate. *Nucl Med Biol* 2004; **31**: 859–65.

ORIGINAL ARTICLE

Automatic laser scanning ablation system for high-precision treatment of brain tumors

Hongen Liao · Keisuke Fujiwara · Takehiro Ando ·
Takashi Maruyama · Etsuko Kobayashi ·
Yoshihiro Muragaki · Hiroshi Iseki · Ichiro Sakuma

Abstract Complete removal of malignant gliomas is important for the prognosis in neurosurgery treatment. Currently, the challenge is how to detect any remaining tumors and resect them during the operation. We have developed a laser ablation system with accurate tumor analysis and fluorescence guidance for high-precision brain tumor resection during neurosurgery. A 5-aminolevulinic acid-induced fluorescent protoporphyrins IX (PpIX)-based intra-operative fluorescence measurement and corresponding spectra analysis technique is used to identify the position of tumors. A galvano mirror scanning mechanism is integrated into the fluorescence measurement and the laser ablation devices for automatic tumor area scanning and corresponding laser ablation. A set of phantom experiments was performed to evaluate the proposed system. Results showed that the galvano scanning mechanism enabled both PpIX fluorescence detection and laser ablation in the same optical axis. In vitro experiments using porcine brain were performed to evaluate the effectiveness of the automatic laser scanning, fluorescence detection, and laser ablation system. The proposed fluorescence-guided laser ablation system can provide accurate analysis and high-precision treatment for tumor resection in neurosurgery. With further improvement, the system can be used in neurosurgical implementation to provide accurate, safe, and simple surgical diagnosis and therapy.

H. Liao (✉) · K. Fujiwara · T. Ando · E. Kobayashi · I. Sakuma
Graduate School of Engineering, The University of Tokyo,
7-3-1 Hongo, Bunkyo-ku,
Tokyo 113-8656, Japan
e-mail: liao@bmpe.t.u-tokyo.ac.jp

H. Liao · E. Kobayashi · I. Sakuma
Translational Systems Biology and Medicine Initiative,
The University of Tokyo,
7-3-1 Hongo, Bunkyo-ku,
Tokyo 113-8656, Japan

H. Liao
School of Medicine, Tsinghua University,
Beijing 10084, China

T. Maruyama · Y. Muragaki · H. Iseki
Graduate School of Medicine,
Tokyo Women's Medical University,
8-1 Kawada-cho, Shinjuku-ku,
Tokyo 162-8666, Japan

Introduction

Malignant gliomas are the most common type of primary brain tumor. While primary malignant brain tumors account for just 2 % of all adult cancers, these tumors cause a huge burden in long-term of disability and death [1]. The symptoms, prognosis, and treatment for malignant gliomas depend on the cell type, grade of malignancy, and location of tumor within the brain. Determining how to completely remove malignant gliomas during neurosurgery is crucial because it affects the overall prognosis of the treatment. Surgeons can resect

🖄 Springer

Fig. 1 System configuration
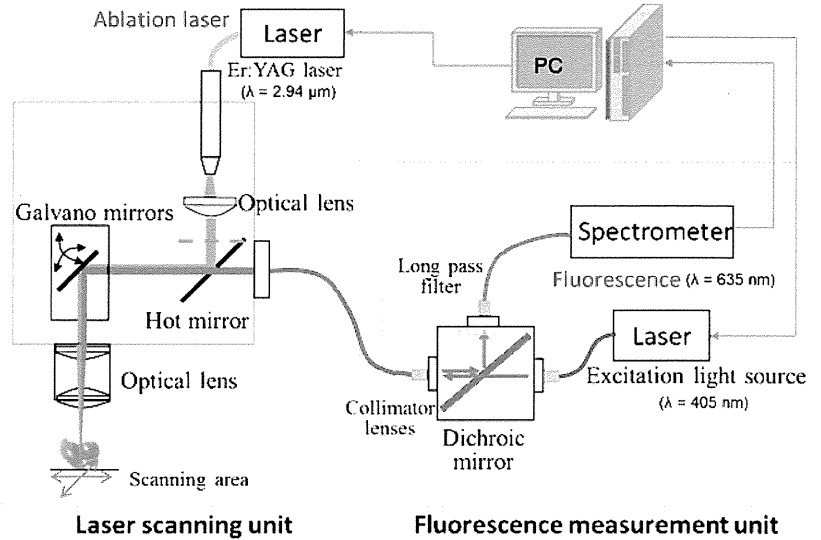
most tumors with an accuracy of millimeters by using a combination of conventional surgical instruments and diagnostic images [2, 3]. Although magnetic resonance (MR) and computed tomography (CT) images can provide surgeons with pre-/intra-operative diagnosis information, some tumor cells remain in the areas adjacent to the tumor removal area and can negatively affect both the diagnosis outcome and the precision of the treatment. It is not enough for surgeons to distinguish the edges of the tumor only using conventional surgical techniques because of the uncertainty involved in identifying viable tumor margins during surgery. In order to perform a complete tumor resection, the accuracy of intra-operative tumor detection and diagnosis needs to be improved.

In a previous study, a 5-aminolevulinic acid (5-ALA)-induced protoporphyrins IX (PpIX) fluorescence was used for intra-operative visualization of malignant glioma tissue [4]. Using the 5-ALA leads to intracellular accumulation of fluorescent PpIX in malignant gliomas and enables intra-operative visualization of malignant gliomas tissue. Other studies have shown that fluorescence can be used to identify residual malignant glioma intra-operatively, thus improving the accuracy of surgical treatment [5–8]. With the guidance of 5-ALA-induced fluorescence in neurosurgery, surgeons can resect a tumor more accurately and intuitively [9, 10].

To achieve a complete resection of tumor tissue, tumor ablation accuracy during treatment is required. The use of laser ablation enables a smooth, precise treatment for small and/or remaining tumors [11]. Laser photocoagulation provides a noncontact therapeutic method with a sub-millimeter accuracy [12, 13]; moreover, the power and the photocoagulation time of the

laser is easy to control, thus enabling a more complete tumor removal.

An integrated diagnosis and therapeutic system has been developed for high-precision malignant glioma resection using a 5-ALA-induced fluorescence PpIX-based intra-operative tumor diagnosis technique combined with a laser ablation technique that features an autofocus (AF) mechanism [14, 15]. The boundary between tumorous and nontumorous tissue is identified using 5-ALA-induced PpIX fluorescence and the tumor is then accurately ablated with the micro laser. Combining the 5-ALA fluorescence guidance with high-precision spectral analysis results in higher tumor identification accuracy than with a system that uses only pre-/intra-operative MR imaging [16]. However, the fluorescence
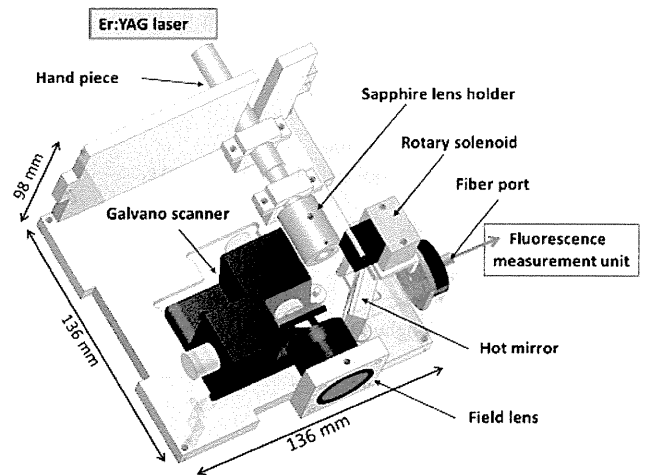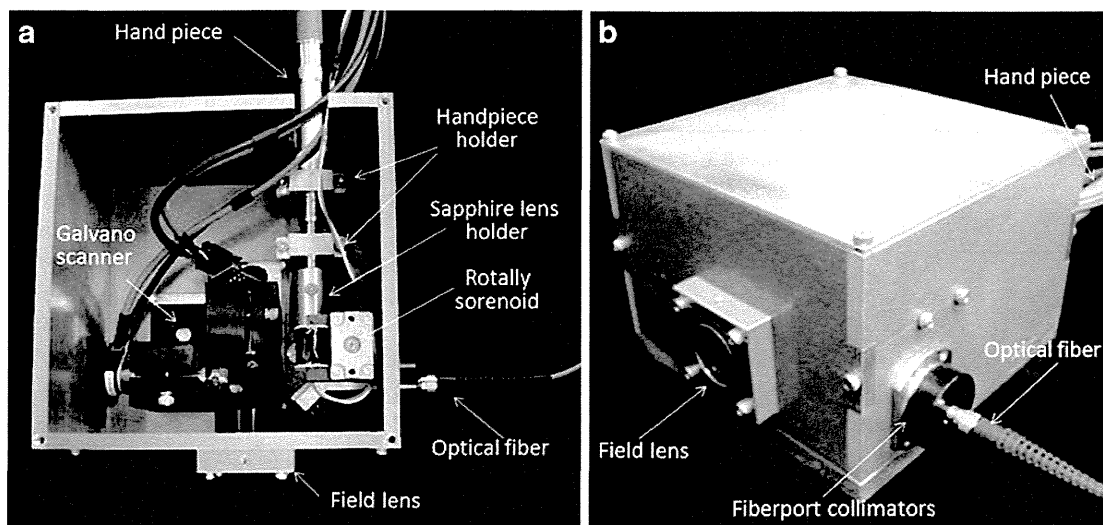

Fig. 2 Design of laser scanning unit

Fig. 3 Manufactured laser scanning unit. **a** Galvano scanning mechanism and laser ablation guidance device; **b** compacted laser scanning unit that can be mounted to a robotic arm during neurosurgery

measurement device and the laser ablation device were separated. The entire tumor was first scanned and the tumor area was indentified. Laser ablation was performed after fluorescence spectral analysis. Although experiments have demonstrated that it is possible to use an AF device mounted on a robotic manipulator, the spectral analysis and laser ablation could not be performed simultaneously. Because deformation and movement of the brain tissue occurs during the surgical procedure, the nonsimultaneous preformation of diagnosis and therapy affects the accuracy of tumor resection.

To address these issues, we developed a new mechanism with the same optical path for the excitation laser used in fluorescence measurement and the ablation laser used for tumor laser photocoagulation. Our coaxial system includes

an automatic laser scanning mechanism for automatic fluorescence measurement and laser ablation when the direction of the lasers is needed to be changed. The rest of this paper is organized as follows. In the "Methods and system configuration" section, we describe the requirements of fluorescence-guided laser ablation for neurosurgery, the system configuration, and the details of each unit. In the "Experiments and results" section, we present our automatic laser scanning ablation device and a set of experiments we performed to assess the laser photocoagulation as well as our analysis of the fluorescence spectra. An in vitro experiment using porcine brain tissue is also described in this section. We discuss possible extensions to the method and conclude with a brief summary in "Discussion and conclusion" section.
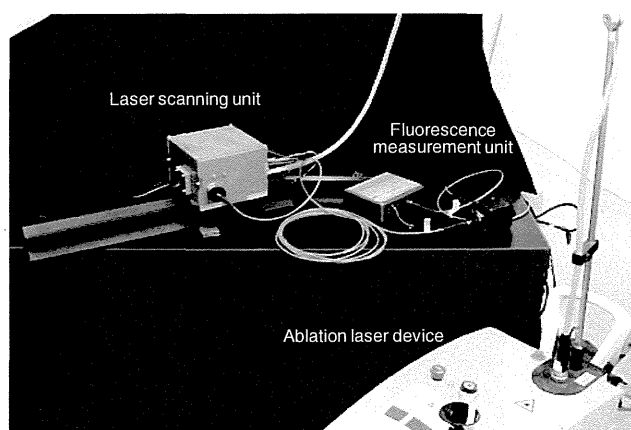
Methods and system configuration

We develop a coaxial fluorescence measurement with and laser ablation system for accurate analysis of tumor and high-precision brain tumor resection during neurosurgery. In this section, we describe the system requirements related to fluorescence-guided laser ablation for neurosurgery, the system configuration, the fluorescence measurement and analysis, the laser scanning mechanism, and the laser ablation device.

Requirements of fluorescence-guided laser ablation for neurosurgery

Although combining diagnosis imaging techniques (such as MRI and CT) can improve tumor acquisition,

Fig. 4 Prototype of the fluorescence measurement and laser ablation device

Table 1 Laser power transmission efficiency (*n*=10)

Positions of Er: YAG laser	20 Hz– 50 mJ	20 Hz– 75 mJ	20 Hz– 100 mJ	10 Hz– 100 mJ
Tip of hand piece	99.6±0.5	97.2±0.4	98.2±0.3	98.2±0.4
Sapphire lens	85.8±0.5	85.3±0.4	85.8±0.5	86.4±0.6
Objective lens	66.9±0.5	65.4±0.3	66.6±0.4	67.2±0.6

performance, accurate, real-time tumor identification is still required. Using 5-ALA-induced PpIX fluorescence enables high-precision identification of the tumor surface, which is then used to precisely identify small tumors or residual tumor tissue during an operation, thereby providing guidance for laser ablation. With the integration of a laser ablation device, the system can be used for precision intra-operative treatment for blurry boundaries between healthy brain tissue and brain tumor that may contain a tumor. There are four main requirements for using fluorescence-guided laser ablation in neurosurgery: (1) the working distance from the scanning plane should be about 20 mm, (2) the laser scanning unit should be mounted on a neurosurgery robotic arm in the operation room, (3) the laser scanning range for small tumors should be about 10 mm×10 mm, (4) the diameter of the laser spot ablated on the tumor should be less than 2 mm, and (5) laser photocoagulation should only be performed on a tumor with the guidance of fluorescence.

System configuration

The proposed fluorescence-guided automatic laser ablation system includes a fluorescence measurement unit, a laser scanning unit, and a PC for fluorescence spectra

analysis and ablation laser control (Fig. 1). The PC is used to control the fluorescence measurement and laser scanning units. Data received from a spectrometer is also analyzed by the PC. These analyzed results are then used to determine whether or not the scanned area is tumor tissue. The laser scanning unit has two functions: one for fluorescence measurement scanning and the other for laser ablation scanning. The laser scanning and tumor ablation procedure consists of four parts: (1) an excitation light (blue–violet light, λ=405 nm) is used to excite the PpIX so that a brain tumor is easy to spot by the red fluorescence it emits, (2) a spectroscope is used to collect excited fluorescence, which is then analyzed by PC, (3) if the area is identified as containing tumor tissues, a hot mirror is angled downward so that the Er:YAG laser can be trained on the target area, and (4) the fluorescence analysis and laser ablation procedure with the galvano mirror scanning mechanism are repeated so that all the required area can be scanned.

Fluorescence measurement unit

As a metabolic precursor in the heme biosynthesis pathway, 5-ALA elicits and induces the synthesis of PpIX, which tends to accumulate in pathological lesions. When it is excited by blue-violet light (wavelength of about 405 nm), brain tumors are easy to spot due to the PpIX emitting a red fluorescence (wavelength of about 635 nm). In this system, we selected a laser diode with a wavelength of 406 nm (GH04125A2AE, SHARP Co., Maximum output: 150 mW) connected by a fiber as a light source. A spectrometer (WTC-111E; B&W TEK Inc.; wavelength measurement range, 300–850 nm) was used to measure the spectrum. The exposure time of the spectrometer can be controlled by PC. We use a

Fig. 5 Laser photocoagulation efficiency with same repetition frequency (20 Hz) and different pulse energies (30, 50, 75 mJ/pulse)
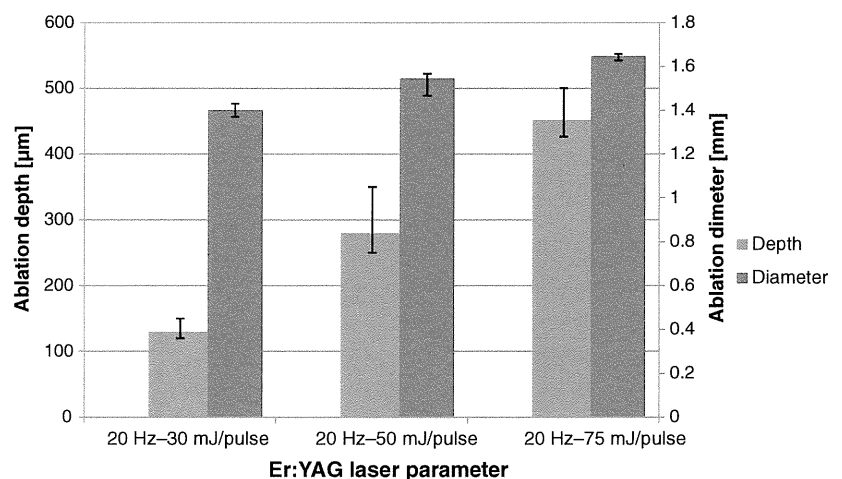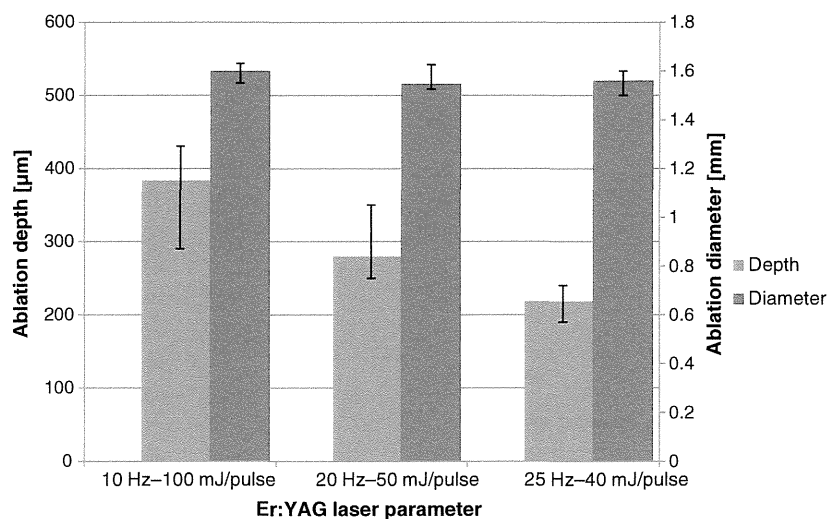
Fig. 6 Laser photocoagulation
efficiency with different
repetition frequencies and pulse
energies. The total laser power
output was the same

dichroic mirror (cutoff wavelength, 550 nm) to combine the optical path for optical fiber (core diameter, 365 μm) so that the excitation light and the fluorescence can be guided by a single fiber.

As shown in the fluorescence measurement unit in Fig. 1, the laser scanning unit is connected with the spectrometer and the excitation light source with a fiber. Since the excitation light and the fluorescence are transmitted by the same fiber, the fluorescence is only obtained from the excited area of PpIX. In order to decrease the strong reflected excitation light that cannot be avoided by dichroic mirror, we inserted a long pass filter with a cutoff wavelength of 550 nm between the mirror and the spectrometer.

Laser scanning unit

Figure 2 shows the design of the laser scanning unit. An Er:YAG laser device (ER-M1TH; HOYA Photonics

Inc.) was used for tumor laser photocoagulation. This device enables a laser output of oscillator pulse repetition frequency (selectable from 3, 10, 20, 25, or 30 Hz) and pulse energy (30–350 mJ/pulse). A galvano mirror scanner (6220 H, Cambridge Technology Inc.) was integrated into the laser scanning mechanism. The direction of the excitation light and the Er:YAG laser can be changed by the controlling the angle of the galvanometer mirror so that the tumor area can be scanned automatically without changing the position and orientation of the entire device.

A hot mirror (gold mirror) is placed in front of the galvanometer scanner to switch the optical path. During the fluorescence measurement, the mirror is angled upward so that the fluorescence can pass through the fluorescence measurement unit to the galvano scanning device directly. In the laser photocoagulation procedure, the mirror is angled downward so that the ablation laser can be reflected to the galvano scanning

Fig. 7 Fluorescence measurement for different points; **a** experimental device; **b** measurement points
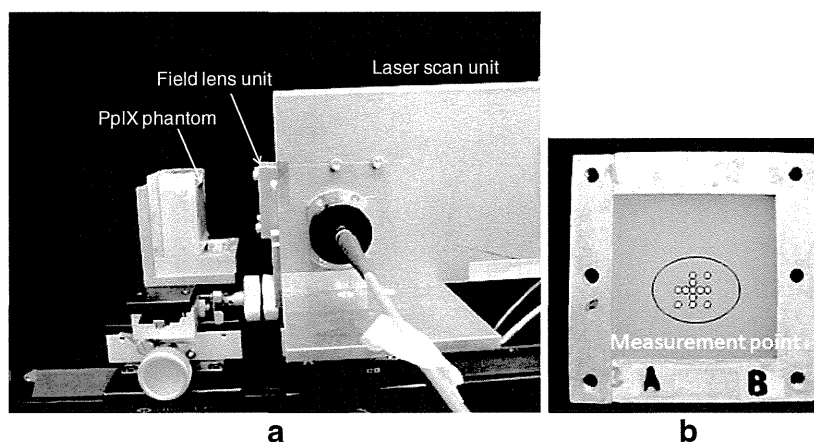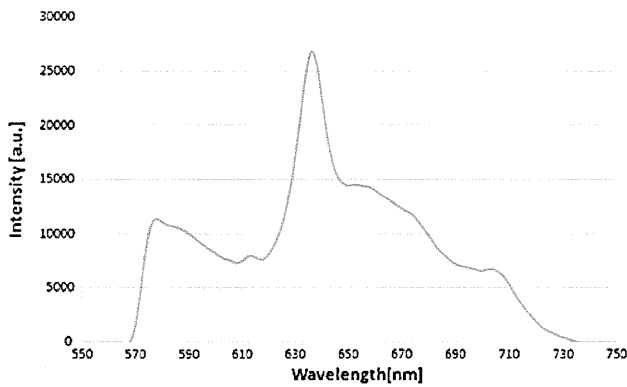
**Fig. 8** Results of fluorescence spectrum

device. When the light from the galvano mirror passes through the objective lens and is irradiated to the target surface, although the two lights have the same angle during both the fluorescence measurement and the laser ablation, they have different focus points due to the chromatic dispersion caused by the large difference in wavelength. We should be able to correct the irradiation angle of the Er:YAG laser by enlarging the irradiation slightly. The optimum correction angle can be determined by ray tracking simulation.

The manufactured laser scanning mechanism is shown in Fig. 3a. The device is compact enough to be mounted on a robotic arm during neurosurgery (Fig. 3b).

Experiments and results

We manufactured the laser scanning device and combined it with the fluorescence measurement device (Fig. 4). A set of experiments were then performed to evaluate the system using a biomedical stimulant phantom and a porcine brain. During experimentation, the developed laser scanning unit was fixed to an optical rail.
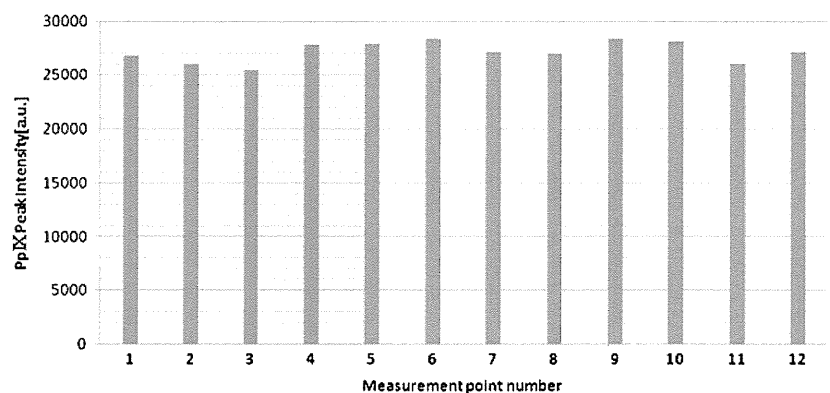
Evaluation of Er:YAG laser power transmission efficiency

First, we evaluated the stability of the Er:YAG laser emitted from the objective lens of the laser scanning unit. The transmission efficiency of the laser power was also measured at three positions: tip of hand piece, sapphire lens, and output position after passing the objective lens. Four combinations of different repetition frequencies and pulse energies (20 Hz–50 mJ, 20 Hz–75 mJ, 20 Hz–100 mJ, 10 Hz–100 mJ) were carried out to evaluate the laser power output. Each test of 5 s per irradiation was performed for 10 measurements.

The results of the laser power measurements are shown in Table. 1. About 65–67 % laser power was transmitted to the target surface regardless of the parameter setting which indicates that the laser power transmission efficiency was stable. In addition, the theoretical value of the transmission efficiency of the laser power was also about 69 %, which is almost equal to the transmission efficiency we experimentally obtained.

Evaluation of Er:YAG laser photocoagulation efficiency

To evaluate the Er:YAG laser photocoagulation efficiency with different repetition frequencies and pulse energies, we constructed a biomedical phantom that could simulate the optical scattering properties of brain tissue. The Er:YAG was applied to the phantom, and we then measured the size and depth of the hole created by the laser irradiation. Five sets of experiments with different combinations of repetition frequency and pulse energy (20 Hz–30 mJ, 20 Hz–50 mJ, 20 Hz–75 mJ, 10 Hz–100 mJ, 25 Hz–40 mJ) were performed.

Figure 5 shows the results of the Er:YAG laser photocoagulation efficiency evaluation. In the case of repetition frequency of 20 Hz, the depth and diameter of the irradiation spot were increased by the increased pulse

Fig. 9 PpIX peak intensity for 12 measurement points